

Ultra-Small Ferromagnetic Fe₃O₄ Nanoparticles Modified Separator for High-Rate and Long Cycling Lithium-Sulfur Batteries

Wence Yue,^[a, b] Xue Li,^[b] Jie Zhao,^[b] Yibo Gao,^[b] Ning Gao,^[b] Bao Li,^[c] Guangming Xia,*^[a] Shumin Zheng,*^[b] and Bao Wang*^[b]

As a promising energy storage system with high specific capacity, lithium-sulfur (Li–S) battery is striving for a high-rate and longer lifetime. Whereas the slow redox kinetics and the shuttle effect of polysulfides (PSs) still severely restrict the performance of Li–S batteries. Here, a rational designed ferromagnetic Fe₃O₄ nanoparticles (FM-Fe₃O₄ NPs) modified separator is engineered for Li–S batteries. Moreover, the particle size of FM-Fe₃O₄ NPs was tuned to enhance the energy storage performance. Consequently, the cells with FM-Fe₃O₄ NPs modified separator achieved a high-rate and long cycling performance, the specific capacity could reach 672.8 mAh g⁻¹ and a low fading rate (0.028% per cycle over 700 cycles) at a

high rate of 5 C. Experimental results reveals that FM-Fe₃O₄ NPs could mitigate shuttle effect, enable efficient redox reactions, and protect the Li anode from severe corrosion. The performance-enhanced mechanism is further discovered by DFT calculations, the results show that FM-Fe₃O₄ NPs act as mediators of redox reaction to block PSs shuttle and dynamically facilitate conversion via changing the molecular structure of PSs and reducing reaction barrier. This work provides a new pathway to improving Li–S batteries based on ferromagnetic materials, which may be generalized to other advanced batteries.

Introduction

Lithium-sulfur (Li–S) batteries emerged as a promising candidate for next-generation energy storage systems due to high theoretical energy density (2567 Wh kg⁻¹), high theoretical capacity (1675 mAh g⁻¹), low cost, and environmental friendliness.^[1–3] As portable electronic devices and electric vehicles are becoming ubiquitous, rechargeable batteries with high-rate and long cycling stability are desired for the energy storage market.^[4–6] However, the rate and cycling performance of Li–S batteries are restricted by the insulator nature of sulfur and Li₂S/Li₂S,^[7,8] serious volume change of sulfur during the redox conversion process,^[9] and the shuttle effect.^[10]

To overcome the above problems, the current effort is often dedicated to the search for new host materials, including carbon materials,^[11–13] metal oxides,^[14–16] metal sulfides,^[17,18] and metal nitrides.^[19–22] Few reports can be found on the research of separator and interlayer,^[23] binder^[24,25] and electrolyte.^[26] Among them separator is a critical component that determines short-circuiting between the cathode and the anode. Thus, modifying the commercial polypropylene (PP) separators with effective materials can promote the block, adsorption, and catalytic conversion abilities for polysulfides (PSs), hence can synchronously suppress the shuttle effect of soluble PSs and accelerate the transmission of lithium-ion.

In recent years, nanomaterials have been widely used in Li–S batteries.^[27–29] Nanomaterials would provide better adsorption and catalytic performance due to increased surface area and abundant active sites. In this work, we engineered a ferromagnetic Fe₃O₄ nanoparticle (FM-Fe₃O₄ NPs) modified separator for Li–S batteries. The FM-Fe₃O₄ NPs have high conductivity^[30,31] and strong chemical interaction with PSs.^[32,33] The particle size of FM-Fe₃O₄ NPs was tuned to enhance the performance of Li–S batteries because the decreasing size of Fe₃O₄ nanoparticles would provide better adsorption and catalysis performance due to the increased surface area and abundant active sites.^[34,35] 6, 12, and 20 nm FM-Fe₃O₄ NPs were fabricated. Nevertheless, the reduction in nanoparticles size also brings higher surface energy to the nanoparticles, which causes aggregation of nanoparticles. To avoid the above-mentioned problem, FM-Fe₃O₄ nanoparticles are first prepared and then directly anchored on the surface of CNTs (Fe₃O₄@CNTs),^[36] which not only improves the conductivity but also effectively prevents the aggregation of FM-Fe₃O₄ nano-

[a] W. Yue, Prof. Dr. G. Xia
School of Chemistry and Chemical Engineering
University of Jinan
Jinan 250022, China
E-mail: chm_xiagm@ujn.edu.cn

[b] W. Yue, X. Li, J. Zhao, Y. Gao, N. Gao, Dr. S. Zheng, Prof. Dr. B. Wang
State Key Laboratory of Biochemical Engineering Institute of Process Engineering
Chinese Academy of Sciences
No. 1 Beierjie, Zhongguancun, Beijing 100190, China
E-mail: smzheng@ipe.ac.cn
baowang@ipe.ac.cn

[c] B. Li
School of Chemistry and Chemical Engineering
Henan Normal University
Xinxiang, Henan, 543007, China

 Supporting information for this article is available on the WWW under
<https://doi.org/10.1002/batt.202200020>

 An invited contribution to a Special Collection dedicated to Lithium–Sulfur Batteries

particles. DFT calculation was introduced to further discover the performance-enhanced mechanism, the results show that FM- Fe_3O_4 NPs act as mediators of redox reaction to block PSs shuttle and dynamically facilitate conversion via changing the molecular structure of PSs and reducing the reaction barrier. Consequently, the separator modified with 6 nm FM- Fe_3O_4 NPs shows superior performance, a high capacity of 672.8 mAh g⁻¹ was achieved and maintains a high reversible specific capacity of 461.1 mAh g⁻¹ after 700 cycles at a high rate of 5 C. The rational-designed separator restrains the aggravated shuttle effect, and simultaneously accelerated the transmission of lithium-ion, thus enables a high-rate and long cycling Li-S battery.

Experimental

Materials

Iron chloride ($\text{FeCl}_3 \cdot 6\text{H}_2\text{O}$, 98%, Aldrich) Sodium oleate ($\text{C}_{18}\text{H}_{33}\text{NaO}_2$, 97%, TCI), n-Hexane (AR, Macklin), Acetone (AR, SCR), Oleic acid (AR, Aladdin), Diphenyl ether (AR, Macklin), 1-Octadecene (GC, Macklin), Trioctylamine (95%, Aladdin).

Synthesis of Fe_3O_4 nanoparticles

Monodisperse OA-capped Fe_3O_4 nanoparticles were synthesized by the modified method in this work.^[37] Firstly, iron oleate was synthesized by the reaction between sodium oleate and iron chloride. And then iron oleate and OA were dissolved in the solvent in a three-neck flask at room temperature. Subsequently, the mixture was heated at boiling point for 1 h under N_2 atmosphere. After cooling down to room temperature, the Fe_3O_4 nanoparticles were washed with acetone and hexane. Finally, the OA- Fe_3O_4 nanoparticles with 6, 12, and 20 nm were obtained. The nanoparticles of different sizes were controlled by solvents with different boiling points.

Synthesis of $\text{Fe}_3\text{O}_4@\text{CNTs}$

OA- Fe_3O_4 of 100 mg and CNTs of 50 mg were dispersed in 30 mL n-hexane followed by ultrasonication. After magnetic stirring, the mixture solution was dried at 70 °C in an oven. The $\text{Fe}_3\text{O}_4@\text{CNTs}$ composites were obtained after carbonization at 600 °C for 2 h under Ar atmosphere.

Fabrication of $\text{Fe}_3\text{O}_4@\text{CNTs}$ and CNTs separator

The modified layer of the separator was obtained by the scraper coating method. The slurry was obtained by mixing $\text{Fe}_3\text{O}_4@\text{CNTs}$, Super P, and poly(vinylidene fluoride) (PVDF) in N-methyl pyrrolidone (NMP) with a mass ratio of 8:1:1. Then the slurry was evenly coated on one side of the PP separator. The modified separator was dried in an oven for 12 h at 60 °C to remove NMP. And then the $\text{Fe}_3\text{O}_4@\text{CNTs}$ modified separator was cut into discs with a diameter of 16 mm.

Characterization

The crystal structures of the samples were investigated by X-ray diffraction (XRD, Smartlab). The structure and morphology research was performed by scanning electron microscopy (SEM, JSM-7800)

and transmission electron microscopy (TEM, JEM-2100). The elemental mapping was characterized by the energy-dispersive spectroscopy (EDS) module of the SEM apparatus. The Raman spectra were performed by a Renishaw Raman spectrometer. The values of contact angle were measured on an OCA20 machine (Dataphysics, Germany) at room temperature.

Electrochemical measurements

The electrodes were prepared by a slurry-coating procedure. The cathode material was obtained by mixing S, Super P, and polyvinylidene fluoride (PVDF) with a mass ratio of 7:2:1 in NMP to form a homogeneous slurry. The slurry was uniformly painted on a piece of aluminum foil current collector followed by drying at 60 °C in a vacuum oven overnight. The sulfur loading was ~1 mg cm⁻². The electrolyte consists of 1 M LiTFSI with 2% LiNO₃ in a 1:1 v/v solution of 1,3-dioxolane (DOL) and dimethoxymethane (DME). The lithium metal was used as an anode. The coin-type (CR2032) cells were fabricated in a glove box with Ar atmosphere. Cyclic voltammetry (CV) was evaluated at a voltage range of 1.7–2.8 V with a scan rate of 0.1 mVs⁻¹ using a bio-logic VMP3 electrochemical workstation. Electrochemical impedance spectroscopy (EIS) was measured in a frequency range of 0.01–100 kHz by the same bio-logic VMP3 electrochemical workstation. The electrochemical charging/discharging measurements were performed with a voltage range of 1.7–2.8 V on Neware battery test system.

Results and Discussion

The schematic diagram of FM- Fe_3O_4 NPs modified PP separators is shown in Figure 1. Firstly, the iron oleate is obtained as a precursor of OA- Fe_3O_4 NPs. Secondly, the iron oleate is pyrolyzed at high temperatures to obtain uniform monodisperse OA- Fe_3O_4 NPs which are wrapped by oleic acid. Then, after several purifications with n-hexane and acetone, the OA- Fe_3O_4 mixed CNTs are dispersed in n-hexane by ultrasound followed by stir. And then the $\text{Fe}_3\text{O}_4@\text{CNTs}$ composites are obtained by heat treatment after removing the solvent. The ferromagnetic of $\text{Fe}_3\text{O}_4@\text{CNTs}$ was proved under an external magnetic field (Figure S1). Finally, the modified separator is obtained by coating $\text{Fe}_3\text{O}_4@\text{CNTs}$ on PP ($\text{Fe}_3\text{O}_4@\text{CNTs}/\text{PP}$).

The microstructure of the Fe_3O_4 NPs was characterized using transmission electron microscopy (TEM), high-resolution transmission electron microscopy (HRTEM). As shown in Figure 2(a–c), the particle size of FM- Fe_3O_4 NPs was successfully tuned. FM- Fe_3O_4 NPs exhibit good monodispersed, the average size of the synthesized Fe_3O_4 nanoparticles is about 6, 12, and 20 nm, respectively. In addition, the mean crystalline size D for Fe_3O_4 nanoparticles can be calculated by Scherrer's equation:

$$D = k\lambda/\beta\cos\theta$$

where $k=0.89$, λ (0.15405 nm) is the X-ray wavelength of Cu target materials, β is the corrected half-width of diffraction peak, and θ represents the diffraction angle. The average crystal sizes of FM- Fe_3O_4 are 4.6, 12.2 and 18.7 nm, respectively, which are basically consistent with the nanoparticle sizes observed by TEM.

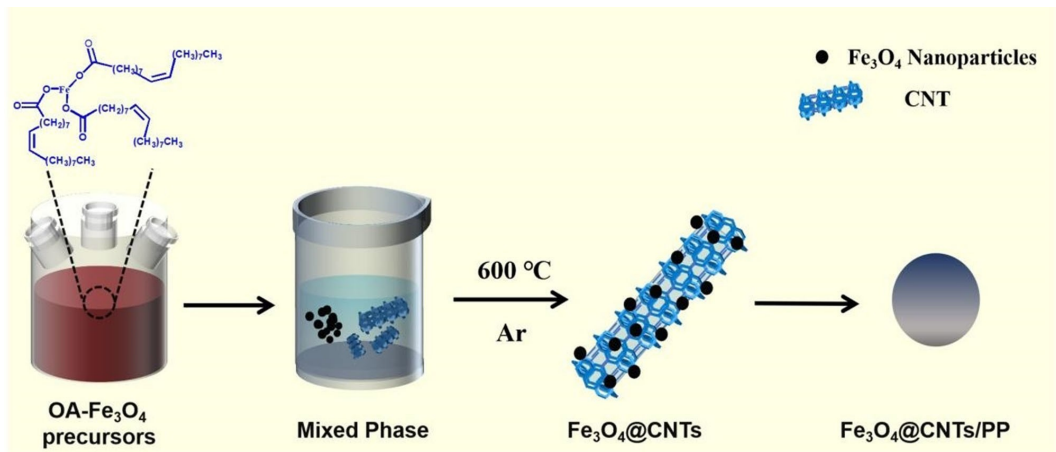


Figure 1. Schematic illustration of the structure of Fe_3O_4 @CNTs modified PP separator.

Energy-dispersive (EDS) mapping of FM- Fe_3O_4 NPs reveals that Fe and O elements were distributed in the sample area (Figure S2). As shown in Figure 2(d–f), FM- Fe_3O_4 NPs anchored on the surface of the CNTs (Figure S3) were observed. The average diameter of FM- Fe_3O_4 NPs remains the value of 6, 12, and 20 nm, respectively. High-resolution TEM (HRTEM) analysis of the FM- Fe_3O_4 NPs (Figure 2g and h) reveals a lattice spacing of 0.213 and 0.260 nm in accordance with the (400) and (311) lattice planes of Fe_3O_4 . The selected area electron diffraction (SAED) pattern of FM- Fe_3O_4 NPs (Figure 2i) shows concentric diffraction rings corresponding to (220), (311), (400), (422), (511), (440) and (533) planes, respectively.

Figure 2(j) shows the digital image of Fe_3O_4 @CNTs/PP separator. The Fe_3O_4 @CNTs/PP separator shows a uniform black color, indicating that Fe_3O_4 @CNTs composites are uniformly coated on PP. The corresponding SEM images further confirm that the Fe_3O_4 @CNTs (Figure 2j) and CNTs (Figure S4) modified-layer are uniformly coated on one side of the commercial PP separator. Moreover, Fe_3O_4 @CNTs did not penetrate the PP separator during the preparation process (Figure S5). The cross-sectional morphology of Fe_3O_4 @CNTs/PP shows the thickness of the Fe_3O_4 @CNTs modified layer is $\sim 15 \mu\text{m}$, as shown in Figure 2(k). The corresponding EDS elemental mapping images exhibit a homogeneous distribution of C, Fe, and O elements in the modified layer. In addition, Fe_3O_4 @CNTs/PP shows good bending performance. As shown in Figure S6, there is no mechanical delamination under bending, indicating the mechanical durability of Fe_3O_4 @CNTs/PP.

The XRD patterns of Fe_3O_4 @CNTs (bare CNTs without FM- Fe_3O_4 NPs denoted as CNTs, Fe_3O_4 @CNTs with 6, 12, and 20 nm FM- Fe_3O_4 NPs denoted as FC-6, FC-12, and FC-20, respectively) were recorded to identify the composition, as shown in Figure 3(a). The broad peak at about 26.0° in XRD patterns is indexed to (002) of the CNTs. (002) peak becomes weaker in FC-6, FC-12, and FC-20, which can be attributed to the addition of FM- Fe_3O_4 NPs. The peaks at 30.4° , 35.6° , 43.4° , 53.9° , 57.5° , and 63.1° can be indexed to the standard diffraction peaks of Fe_3O_4 (JCPDS NO. 19-0629), corresponding to the SAED pattern. There are no other undesirable impurities. Comparing the

Raman spectrum of CNTs, FC-6, FC-12, and FC-20, similar D and G bands were observed (Figure 3b). The intensity ratios (I_D/I_G) of CNTs, FC-6, FC-12, and FC-20 are 0.87, 0.90, 0.87, and 0.89 respectively, reveals a good graphitization degree. Chemical states of Fe_3O_4 @CNTs are investigated by X-ray photoelectron spectroscopy (XPS) analyses. The peaks at 284.8, 711.0, 725.0, and 531.0 eV can be ascribed to C 1s, Fe 2p, and O 1s. Two peaks in high-resolution spectrum C 1s (Figure 3d), corresponding to C–C/ C=C (284.8 eV), C–O (286.9 eV). As shown in Figure 3(e), characteristic peaks of Fe^{3+} 2p_{1/2} (724.8 eV), Fe^{3+} 2p_{3/2} (711.2 eV), Fe^{2+} 2p_{1/2} (722.5 eV) and Fe^{2+} 2p_{3/2} (708.9 eV) are observed, reveals the existence of 2+ and 3+ Fe. The peaks at 530.3, 531.2, and 533.2 eV can be ascribed to O–C, O–H, and O–Fe. Based on the XPS analysis, the amount of Fe in Fe_3O_4 @CNTs was calculated to be 1.82 wt%.

Electrolyte wettability of separators can seriously influence the electrochemical performances of Li–S batteries. To investigate the electrolyte wettability of Fe_3O_4 @CNTs/PP, we drop the same amount of electrolyte on PP, CNTs/PP (CNTs modified PP), FC-6/PP (FC-6 modified PP), FC-12/PP (FC-12 modified PP), and FC-20/PP (FC-20 modified PP) separators, respectively. As shown in Figure S7(a), the electrolyte exhibits poor infiltration to the PP separator with large contact angles. The contact angles of Fe_3O_4 @CNTs/PP are much smaller than that of the PP separator. The enhanced electrolyte uptake can be attributed to the strong interaction between Fe_3O_4 @CNTs and electrolytes. Compared FC-6/PP (Figure S7b), FC-12/PP (Figure S7d), and FC-20/PP (Figure S7e) separators, the electrolyte could infiltrate and spread quicker in FC-6/PP (Figure S7c), this can be attributed to the ultra-small FM- Fe_3O_4 NPs. Importantly, the high electrolyte uptake is beneficial for the diffusion of lithium-ion.

The electrochemical performance of the assembled cells with Fe_3O_4 @CNTs/PP is investigated. The CV curves of CNTs/PP, FC-6/PP, FC-12/PP, and FC-20/PP with a scanning rate of 0.1 mV^{-1} are displayed in Figure 4(a–d). The CV curves contain two cathodic peaks and one anodic peak, where the cathode peak I ($\sim 2.23 \text{ V}$) is the conversion of $\text{S}_8 \leftrightarrow \text{Li}_2\text{S}_4$, the cathode peak II ($\sim 2.01 \text{ V}$) is the conversion of $\text{Li}_2\text{S}_4 \leftrightarrow \text{Li}_2\text{S}_2/\text{Li}_2\text{S}$ and the

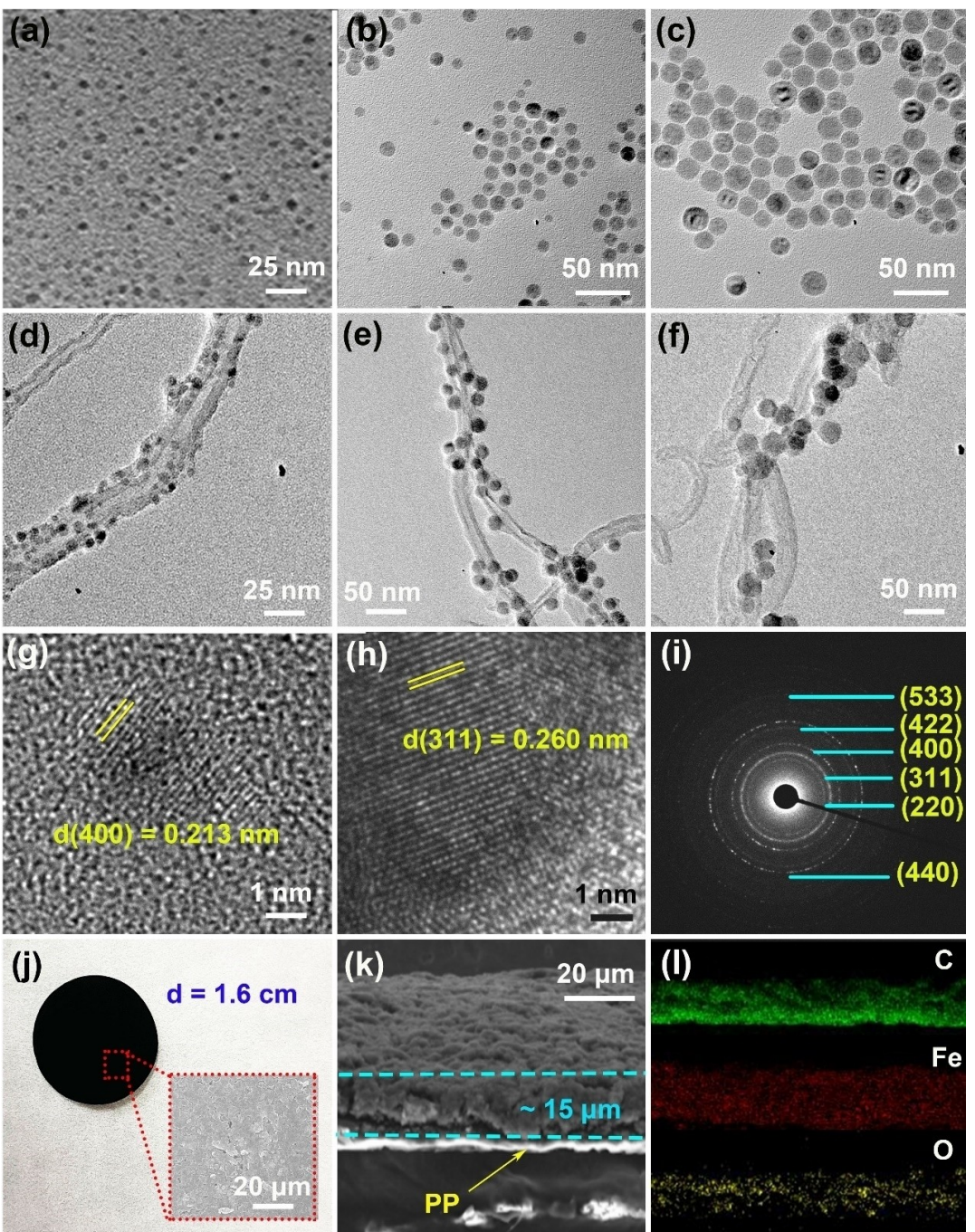


Figure 2. TEM images of FM- Fe_3O_4 NPs. a) 6 nm FM- Fe_3O_4 NPs, b) 12 nm FM- Fe_3O_4 NPs, and c) 20 nm FM- Fe_3O_4 NPs. TEM images of Fe_3O_4 @CNTs with d) 6 nm, e) 12 nm, and f) 20 nm FM- Fe_3O_4 NPs anchored on the surface of CNTs. g and h) HRTEM images of FM- Fe_3O_4 NPs. i) SAED pattern of FM- Fe_3O_4 NPs. j) The digital photographs and SEM image of the Fe_3O_4 @CNTs modified PP separator with the Fe_3O_4 @CNTs coating side; k) side-view SEM image of Fe_3O_4 @CNTs modified PP separator. l) EDS mapping images of C, Fe, O elements in Fe_3O_4 @CNTs modified PP separator.

peak III (~ 2.41 V) is corresponding to the reversed oxidation reaction. The comparison of the CV curves shows that using Fe_3O_4 @CNTs/PP separator could enhance the intensity of redox peaks, which indicates the presence of FM- Fe_3O_4 NPs can greatly mitigate the polarization of cells. The increased cathode peak value and the reduced anode peak prove that Fe_3O_4 @CNTs/PP boost the redox kinetics and improve the reversibility of the cells (Figure S8). The above results show that

the cells with Fe_3O_4 @CNTs/PP separator raise electrochemical performance via reducing electrochemical polarization, boosting redox kinetics, and improving the redox reversibility during cycles.

In addition, the electrocatalytic effect of FM- Fe_3O_4 NPs could also be validated through the change of the onset potential of the redox peak. The corresponding differential CV curves of the cells with different Fe_3O_4 @CNTs/PP separators are

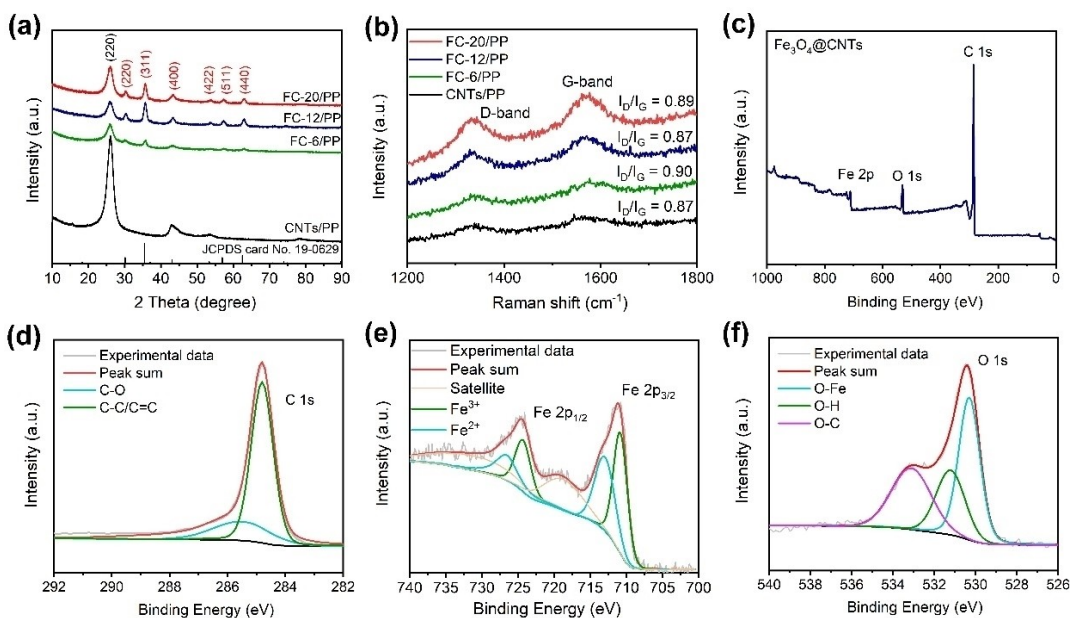


Figure 3. a) XRD patterns of the modified separators. b) Raman spectra of the modified separators; c) XPS spectra of $\text{Fe}_3\text{O}_4@\text{CNTs}$. High-resolution XPS spectra of d) C 1s, e) Fe 2p and f) O 1s.

shown in Figure S9(a-d). In the differential CV curves of the cells, the baseline voltage and current are defined as the values before the redox peaks, where the variation on current is the smallest ($dI/dV=0$). Compared to the cells with CNTs/PP separator (Figure S9a), the cathodic peak onset potential of the FC-6/PP, FC-12/PP, and FC-20/PP increased, while the onset potential of the anodic peak reduced, which indicates that FM- Fe_3O_4 NPs show efficiency in electrocatalytic conversion of PSs, hence enhancing the redox kinetics.

To further reveal the catalytic effect of FM- Fe_3O_4 NPs on the redox of PSs, the symmetrical batteries containing Li_2S_6 are tested by cyclic voltammetry (CV) with a scan rate of 1 mV s^{-1} at a voltage range of -0.8 V to 0.8 V . As shown in Figure 4(e), as the size of the FM- Fe_3O_4 NPs decreases, the current response would increase, which can be attributed to the abundant active sites provided by ultra-small particles for adsorption and catalytic conversion of PSs.^[38] To further investigate the catalytic activity of Fe_3O_4 for polysulfide reduction, potentiostatic nucleation of Li_2S in polysulfides was performed at 2.05 V . As shown in Figure S10 (a and b), $\text{Fe}_3\text{O}_4@\text{CNTs}$ possesses a higher discharging current of 0.81 mA , compared to that of CNTs (0.42 mA). Correspondingly, $\text{Fe}_3\text{O}_4@\text{CNTs}$ shows a higher Li_2S precipitation capacity of 38 mAh g^{-1} (light blue area in Figure S10b) than those of CNTs cathode (14 mAh g^{-1} , yellow area in Figure S10a), suggesting that $\text{Fe}_3\text{O}_4@\text{CNTs}$ layers can accelerate to the nucleation and deposition of $\text{Li}_2\text{S}_2/\text{Li}_2\text{S}$ on their surface.^[39] Besides, the Tafel curves for initial lithiation of symmetrical $\text{Li}_2\text{S}_6-\text{Li}_2\text{S}_6$ cells with CNTs/PP, FC-6/PP, FC-12/PP, and FC-20/PP separators are shown in Figure S11. Cells with FC-6/PP, FC-12/PP, and FC-20/PP separators exhibit higher exchange current and lower polarization potential than the cell with CNTs/PP separator. In addition, the decrease in the size of Fe_3O_4 nanoparticles could further increase exchange current

and reduce polarization potential. This result indicates that the introduction of ultra-small FM- Fe_3O_4 NPs could greatly enhance the redox kinetics of PSs.

The electrochemical impedance spectroscopy was used to analyze the internal impedance of $\text{Fe}_3\text{O}_4@\text{CNTs}/\text{PP}$ cells (Figure 4f). The slopes in the low-frequency area of the $\text{Fe}_3\text{O}_4@\text{CNTs}/\text{PP}$ cells are much higher than those of the CNTs/PP cells, which indicates that they have lower lithium-ion diffusion resistance. Similarly, the semicircular diameter in the high-frequency area of the cells with $\text{Fe}_3\text{O}_4@\text{CNT/PP}$ have much smaller than those of the CNTs/PP cells, which indicates the introduction of FM- Fe_3O_4 NPs would reduce the charge transfer resistance. And it is worth noting that cells with small-size FM- Fe_3O_4 NPs hold smaller semicircular diameters ($R_{\text{FC-6/PP}} < R_{\text{FC-12/PP}} < R_{\text{FC-20/PP}}$), which indicates that the ultra-small FM- Fe_3O_4 NPs could greatly improve the redox kinetics.

The advantages of the fast ion diffusion ability of the $\text{Fe}_3\text{O}_4@\text{CNT/PP}$ were investigated by electrochemical characterizations. Charge/discharge profile at the current densities ranging from 0.1 to 2 C (Figure 5a) has been intensively investigated to evaluate the rate performance of the cells with FC-X/PP separators. The FC-6/PP cell exhibits superior specific capacity at all current densities. The specific capacities are 1261 , 1235 , 1116 , 1038 and 966 mAh g^{-1} at 0.1 C , 0.2 C , 0.5 C , 1 C and 2 C , respectively. More importantly, when the current density returns to 0.2 C , the reversible specific capacity could restore to the value of 1162 mAh g^{-1} . This outstanding rate performance is benefits from the ultra-small FM- Fe_3O_4 NPs, smaller particles could provide more active sites for adsorption and electrocatalysis.

Galvanostatic charge/discharge profiles of $\text{Fe}_3\text{O}_4@\text{CNT/PP}$ at different current rates are shown in Figures 5(b) and S12. For the $\text{Fe}_3\text{O}_4@\text{CNTs}/\text{PP}$ cells, two discharging platforms appear at

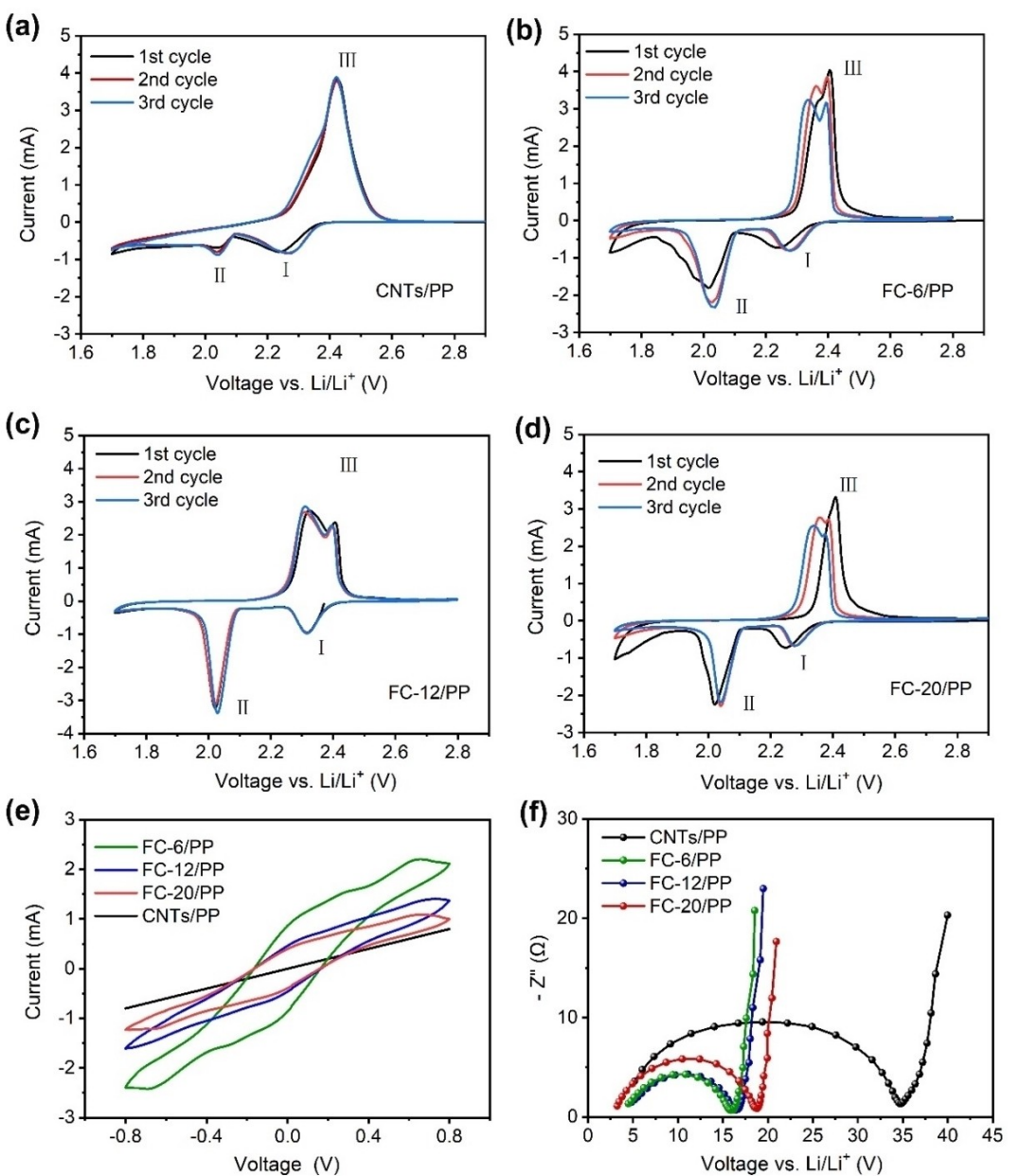


Figure 4. CV curves of cells with a) CNTs/PP, b) FC-6/PP, c) FC-12/PP and d) FC-20/PP separators. e) CV curves of symmetrical $\text{Li}_2\text{S}_6-\text{Li}_2\text{S}$ cells assembly with CNTs/PP, FC-6/PP, FC-12/PP and FC-20/PP at the sweep rate of 1 mV s^{-1} . f) Electrochemical impedance plots of cells with CNTs/PP, FC-6/PP, FC-12/PP and FC-20/PP separators.

~2.33 V and ~2.10 V, and the charging platform appears at ~2.19 V, corresponding to the reduction of soluble long-chain PSs to insoluble $\text{Li}_2\text{S}/\text{Li}_2\text{S}_2$ and their reverse reactions, respectively. Compared to CNTs/PP, the $\text{Fe}_3\text{O}_4@\text{CNTs/PP}$ cells demonstrated an improved capacity at all current densities, among them, FC-6/PP exhibits superior performance. The polarization voltages (ΔE) are ~0.27, ~0.13, ~0.13 and ~0.13 V for CNTs/PP, FC-6/PP, FC-12/PP and FC-20/PP cells, respectively. The smaller polarization voltages and prolonged second discharge plateau for $\text{Fe}_3\text{O}_4@\text{CNTs/PP}$ cells indicate the enhanced kinetics of the conversion from soluble PSs to insoluble $\text{Li}_2\text{S}_2/\text{Li}_2\text{S}$, which can be beneficial to the high capacity.

Figure 5(c) shows the cycle performance of cells using $\text{Fe}_3\text{O}_4@\text{CNTs/PP}$ as separators at 0.2 C. In the first cycle, the specific capacities of the cells with FC-6/PP, FC-12/PP, and FC-20/PP reach 1110 , 1080 , and 1016 mAh g^{-1} , respectively. After 100 cycles, their specific capacities could still reach 979 , 920 , and 893 mAh g^{-1} , the corresponding retention rates are 88% , 85% , and 87% , respectively. The adsorption-catalysis property of FM- Fe_3O_4 NPs efficiently suppresses the shuttle effect, thus enabling a better cycling performance.

Figures 5(d) shows the long-cycle performances of the cells with FC-6/PP separators at high current rates of 2 C and 5 C. The cell with FC-6/PP was activated at a low current rate of 0.1 C. It demonstrates a high specific capacity of 948 mAh g^{-1} at

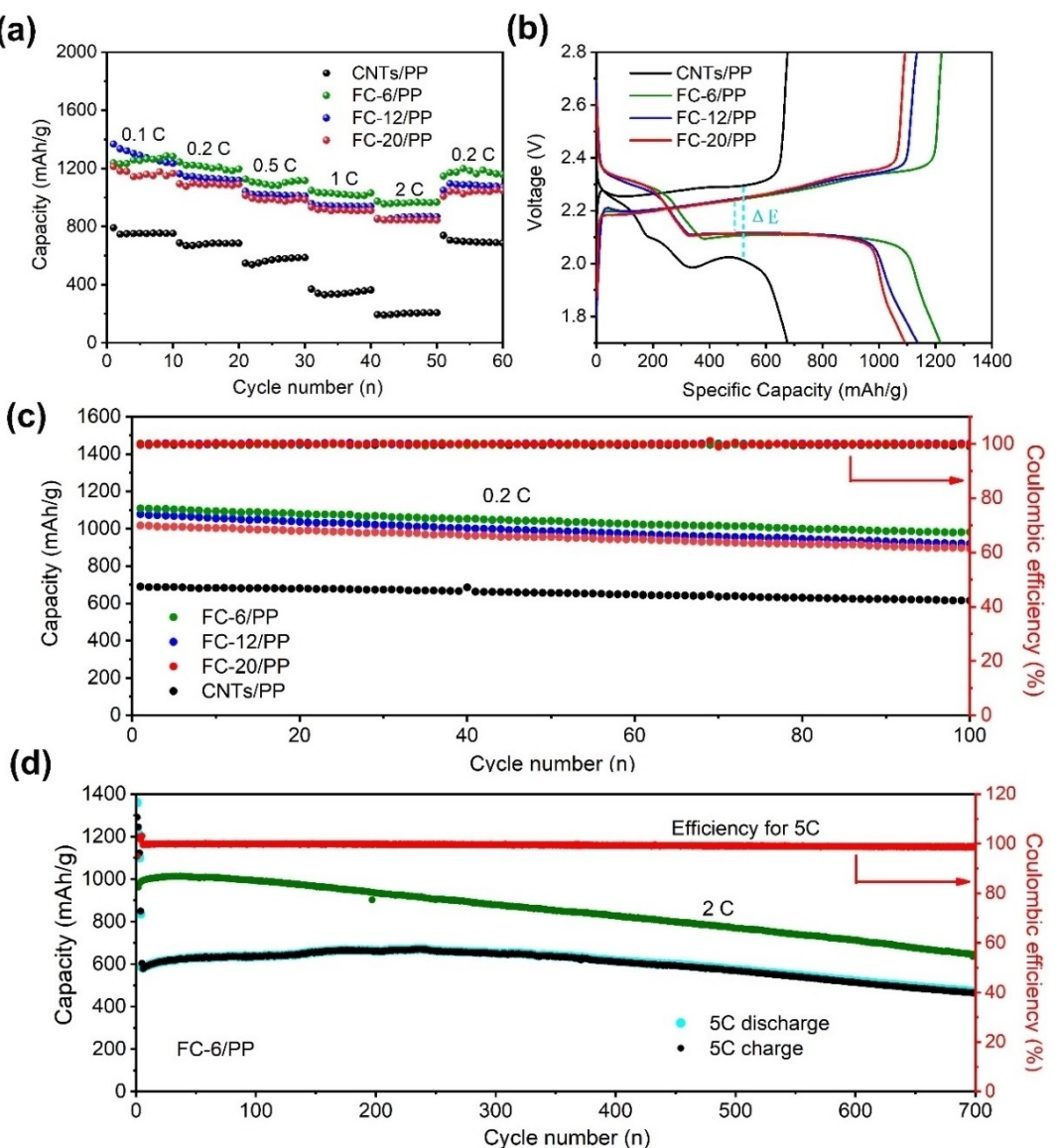


Figure 5. a) Rate performance of cells with CNTs/PP, FC-6/PP, FC-12/PP, and FC-20/PP separators. b) Galvanostatic discharge/charge profiles of cells with CNTs/PP, FC-6/PP, FC-12/PP, and FC-20/PP separators at 0.2 C. Long cycle performances of the cells with FC-6/PP separators at c) 0.2 C and d) 2 C and 5 C.

2 C. Even after 700 cycles, the reversible specific capacity could still reach 652 mAh g^{-1} , and the capacity decay rate of each circle is only 0.045%. Under a higher current density of 5 C, FC-6/PP cells could deliver a high initial discharge capacity of 585 mAh g^{-1} after activation. The reversible specific capacity is 468 mAh g^{-1} after 700 cycles, and the capacity attenuation rate per circle is only 0.028%. Besides the coulombic efficiency is close to 100%. Further pursuing high energy density Li-S batteries, S/CNT cathodes with sulfur content of 70 wt% have been prepared and used to study the electrochemical performance of high sulfur loadings ($\geq 3 \text{ mg cm}^{-2}$). As shown in Figure S13, the initial cycling capacities of the FC-6/PP-modified batteries at sulfur loadings of 3.3 and 4.5 mg cm^{-2} at 0.2 C are 1150 and 815 mAh g^{-1} , respectively. Therefore, even in the case of long-term cycling under a high current rate, the cells can maintain high reversible specific capacity and coulombic

efficiency. The long-term cycling stability with a high S utilization rate indicates that ultra-small FM- Fe_3O_4 NPs could effectively inhibit the shuttle effect of PSs and enables a kinetics efficient charge-discharge process.

In addition, we disassembled the cells after cycling to systematically reveal the morphology variations of the modified separators and Li anodes. Figure 6(a-d) shows the digital photographs of modified separators morphology after cycling. The Fe_3O_4 @CNTs are smoothly anchored on the separator after cycling. In contrast, the modified coating without Fe_3O_4 nanoparticles showed severe chalking and shedding from the separator. As shown in Figure 6(e-h), The SEM images show that the morphology of Fe_3O_4 @CNTs/PP is continuous except for CNTs/PP. Hence, the stable long-term cycle could benefit from the integrity of the structure. As shown in Figure 6(i-l), the digital photographs of Li anode involving with

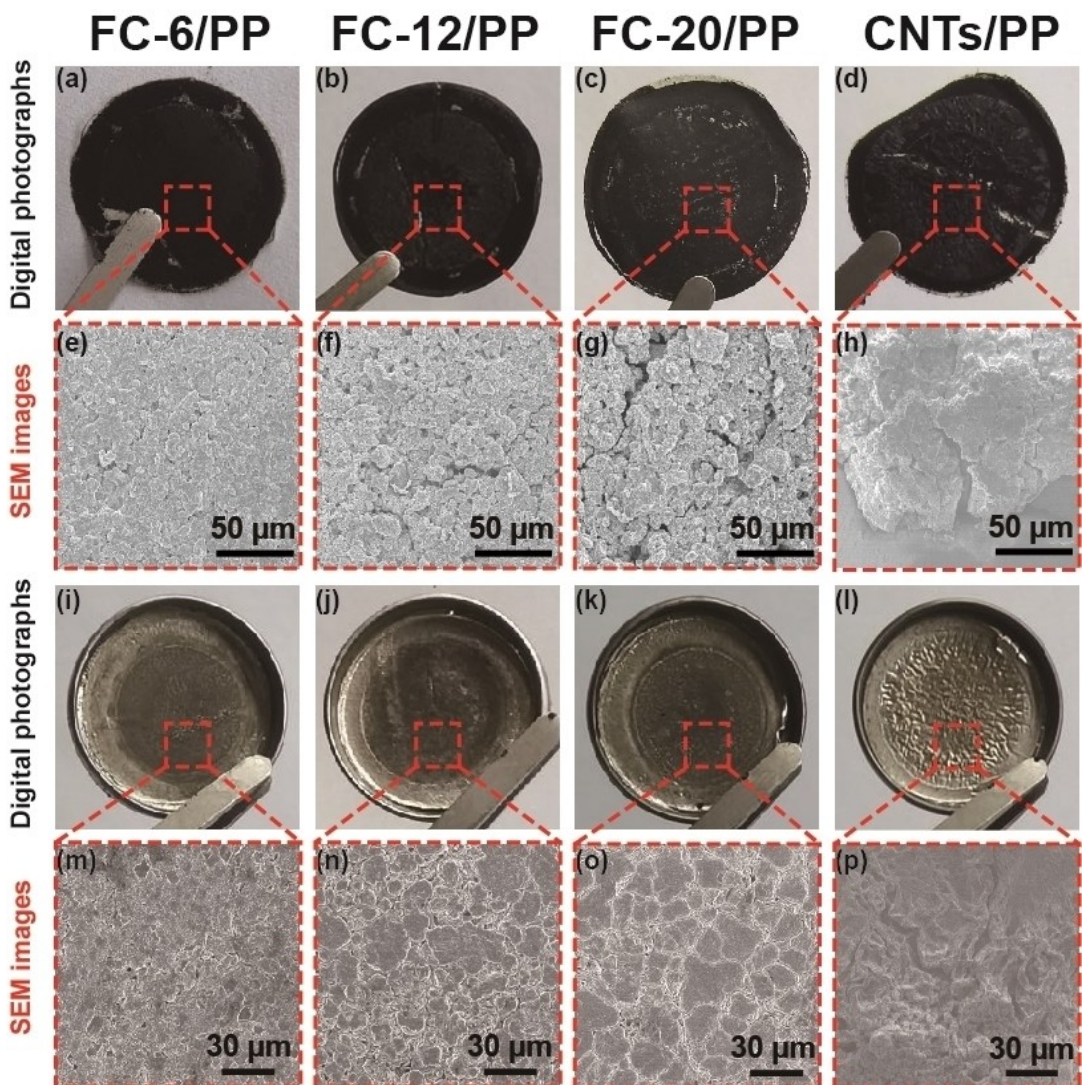


Figure 6. Modified separators morphology of a–d) digital photographs, e–h) SEM images. Li anode surface morphology of i–l) digital photographs, m–p) SEM images for the cells after the cycle.

$\text{Fe}_3\text{O}_4@\text{CNTs}/\text{PP}$ cells have an intact and smooth surface. In contrast, the surface of the Li anode of CNTs/PP cell is rough. The enriched irregular cracks and holes on the Li anode surface of CNTs/PP reveal that Li anode is seriously corroded by PSs, for $\text{Fe}_3\text{O}_4@\text{CNTs}/\text{PP}$ cells, the similar phenomenon is mitigated with the decrease of the particle size of FM- Fe_3O_4 NPs (Figure 6m–p). These results indicate that $\text{Fe}_3\text{O}_4@\text{CNTs}/\text{PP}$ effectively inhibits the shuttle effect of PSs, enables a high reuse of PSs, as well as protects the lithium anode from severe corrosion. Thus, an enhanced long cycling performance is achieved.

The density functional theory (DFT) calculations are conducted to discover the adsorption and catalytic effect of FM- Fe_3O_4 NPs in Li–S. As shown in Figure S14, HRTEM images show that the (400) plane of FM- Fe_3O_4 NPs was detected the most, hence the (400) plane was introduced for DFT calculation. The optimized adsorption configurations of Li_2S_4 molecules on Fe_3O_4 (400) and graphene (001) are shown in Figure 7(a and b).

The adsorption energies (E_a) could be obtained by the following calculations.

$$\begin{aligned} E_a(\text{graphene}-\text{Li}_2\text{S}_4) &= E(\text{graphene}-\text{Li}_2\text{S}_4) - \\ E(\text{graphene}) - E(\text{Li}_2\text{S}_4) &= -0.14 \text{ eV} \\ E_a(\text{Fe}_3\text{O}_4-\text{Li}_2\text{S}_4) &= E(\text{Fe}_3\text{O}_4-\text{Li}_2\text{S}_4) - \\ E(\text{Fe}_3\text{O}_4) - E(\text{Li}_2\text{S}_4) &= -4.58 \text{ eV} \end{aligned}$$

The results show that the (400) plane of Fe_3O_4 NPs could enhance the anchoring effect of sulfur-containing species, which is confirmed by the deformation of Li_2S_4 molecules on the (400) plane. In addition, S atoms in Li_2S_4 molecules tend to combine with Fe atoms to form Fe–S bonds, Li atoms tend to combine with O atoms to form Li–O bonds, which conform to the Lewis acids and bases. Noting that enhanced Li_2S_4 adsorption energy is obtained by Fe_3O_4 (-4.58 eV). To achieve an in-depth understanding of the chemical interaction of Fe_3O_4

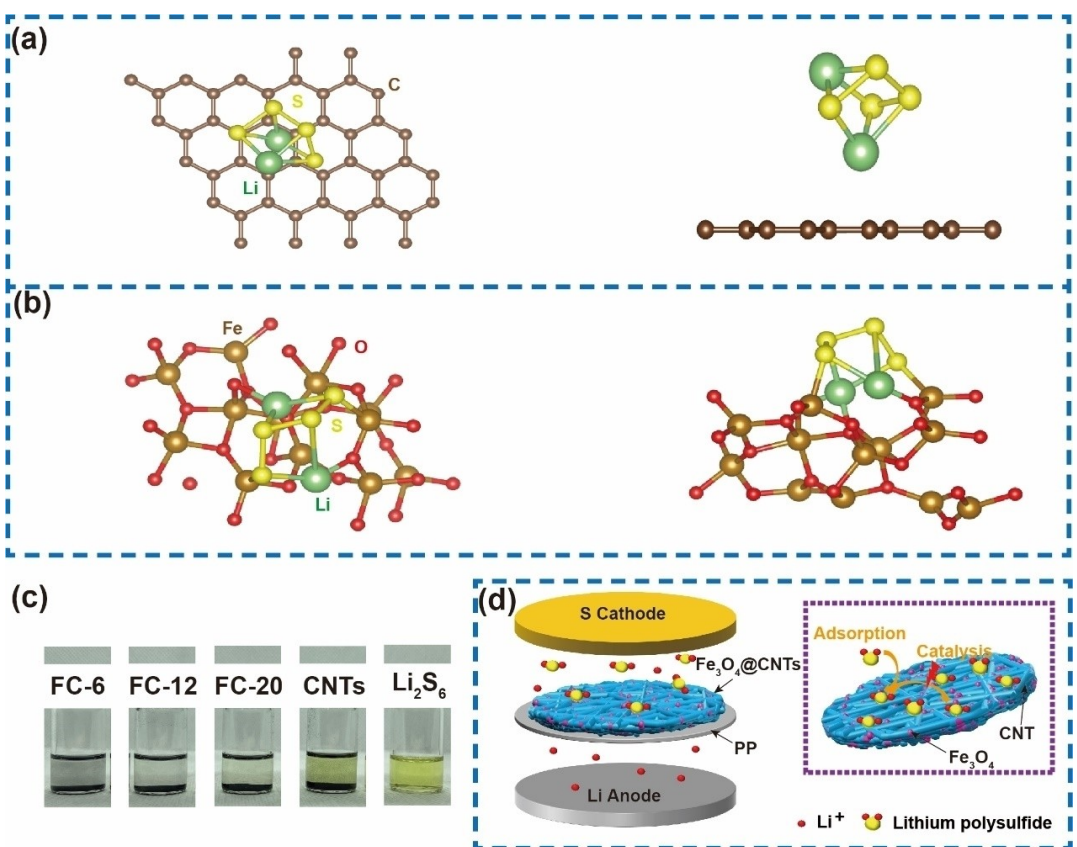


Figure 7. Density functional theory (DFT) calculation of the adsorption energy of Li_2S_4 molecules on a) graphene (001) and b) Fe_3O_4 (400). c) Digital photographs of the color change of the Li_2S_6 -DOL/DME solution in the visualized adsorption experiment. d) Schematic of the electrocatalytic mechanism of $\text{Fe}_3\text{O}_4@\text{CNTs}$ modified separators in Li-S batteries.

and polysulfides, the Fe–S bond in the Fe 2p was measured by XPS spectrum (Figure S15a). As shown in Figure S14(b), the S 2p XPS spectrum (Figure S15b) reveals six sulfur environments with similar peak locations. characteristic peaks of sulfate (170.6 eV), polythionate (168.8 eV), thiosulfate (167.8 eV), Li_2S_2 (163.9 eV) and Li_2S (162.7 eV) are observed. Therefore, it can be concluded that the $\text{Fe}_3\text{O}_4@\text{CNTs}$ modified separator can react more favorably with the polysulfides, providing a more detailed connection with the final discharge products of Li_2S_2 and Li_2S .

To verify the DFT calculated results, the chemical adsorption properties have been studied. As shown in Figure 7(c), the Li_2S_6 visual adsorption experiment is carried out. After 30 min, solutions with the addition of $\text{Fe}_3\text{O}_4@\text{CNTs}$ are nearly colorless, while yellow colors could still be observed in the solution with addition of pure CNTs. In addition, the polysulfide trapping ability of the modified coating was investigated by H-cell configuration (Figure S16). The two chambers of the H-cell configuration are separated by separators (FC-6/PP and CNTs/PP), the right chamber is filled with clear electrolyte while the left chamber is filled with the same electrolyte with yellow Li_2S_6 solution. The solution in the right chamber of the H-cell configuration using FC-6/PP as the separator (Figure S16a) was almost colorless after 24 h, while the solution in the right chamber of the H-cell configuration using CNTs/PP as the separator (Figure S16b) turns yellow after 12 h. This result

shows that the introduction of FM- Fe_3O_4 NPs significantly improves the adsorption performance, which is consistent with the above DFT calculation results. As shown in Figure 7(d), we draft the schematic of the electrocatalytic mechanism of FM- Fe_3O_4 NPs modified separators in Li-S batteries. The $\text{Fe}_3\text{O}_4@\text{CNTs}$ modified coating not only suppresses the shuttle effect through the physical barrier and chemical adsorption but also dynamically facilitates the conversion of the sulfur-containing species. Ferromagnetic materials with ultra-small particles could provide a new path for high-performance Li-S batteries, as well as other advanced batteries.

Conclusion

In summary, the modified separators $\text{Fe}_3\text{O}_4@\text{CNTs}/\text{PP}$ are constructed to successfully suppress shuttle effect and kinetically accelerate PSs conversion, FM- Fe_3O_4 NPs are the effective addition. While the CNTs improve conductivity and ensure electrons transfer in conversion reaction. Consequently, the modified separators with the synergistic effect of electrocatalysis and conductivity lead to an excellent high-rate and ultrastable performance. The cells with FC-6/PP separator could achieve a high specific capacity of 585 mAh g^{-1} at 5 C, and maintain a reversible capacity of 468 mAh g^{-1} after 700 cycles,

the capacity attenuation rate is only 0.028% per circle. The rational-designed construction for separator restrains the aggravated shuttle effect and simultaneously alleviates the loss of sulfur-containing species. Whilst the facile fabrication method will promote the production design for long cycle stability of secondary batteries.

Supporting Information

Supporting Information is available from the Wiley Online Library or from the author.

Acknowledgements

We acknowledge financial support from the 100 Talents Program of Chinese Academy of Sciences, National Natural Science Foundation of China (No. 52172250, 51772296).

Conflict of Interest

The authors declare no conflict of interest.

Data Availability Statement

The data that support the findings of this study are available in the supplementary material of this article.

Keywords: ferromagnetic Fe₃O₄ nanoparticles • high-rate modified separator • DFT calculation • lithium-sulfur batteries

- [1] G. Yan, C. Xu, Z. Meng, M. Hou, W. Yan, N. Lin, L. Lai, D. Zhan, *Nanoscale* **2020**, *12*, 24368–24375.
- [2] C. Yuan, X. Yang, P. Zeng, J. Mao, K. Dai, L. Zhang, X. Sun, *Nano Energy* **2021**, *84*, 105928.
- [3] T. Wang, K. Kretschmer, S. Choi, H. Pang, H. Xue, G. Wang, *Small Methods* **2017**, *1*, 1700089.
- [4] J. Balach, T. Jaumann, M. Klose, S. Oswald, J. Eckert, L. Giebeler, *Adv. Funct. Mater.* **2015**, *25*, 5285–5291.
- [5] R. Li, D. Rao, J. Zhou, G. Wu, G. Wang, Z. Zhu, X. Han, R. Sun, H. Li, C. Wang, W. Yan, X. Zheng, P. Cui, Y. Wu, G. Wang, X. Hong, *Nat. Commun.* **2021**, *12*, 3102.
- [6] H.-J. Peng, J.-Q. Huang, X.-B. Cheng, Q. Zhang, *Adv. Energy Mater.* **2017**, *7*, 1700260.
- [7] Z. Cheng, H. Pan, J. Chen, X. Meng, R. Wang, *Adv. Energy Mater.* **2019**, *9*, 1901609.
- [8] Y. Li, C. Wang, W. Wang, A. Y. S. Eng, M. Wan, L. Fu, E. Mao, G. Li, J. Tang, Z. W. Seh, Y. Sun, *ACS Nano* **2020**, *14*, 1148–1157.
- [9] S. F. Ng, M. Y. L. Lau, W. J. Ong, *Adv. Mater.* **2021**, 2008654.
- [10] S. Huang, Z. Wang, Y. Von Lim, Y. Wang, Y. Li, D. Zhang, H. Y. Yang, *Adv. Energy Mater.* **2021**, *11*, 2003689.

- [11] X.-B. Cheng, J.-Q. Huang, Q. Zhang, H.-J. Peng, M.-Q. Zhao, F. Wei, *Nano Energy* **2014**, *4*, 65–72.
- [12] H. Tang, J. Yang, G. Zhang, C. Liu, H. Wang, Q. Zhao, J. Hu, Y. Duan, F. Pan, *Nanoscale* **2017**, *10* (1), 386–395.
- [13] R. Ummethala, M. Fritzsche, T. Jaumann, J. Balach, S. Oswald, R. Nowak, N. Sobczak, I. Kaban, M. H. Rümmeli, L. Giebeler, *Energy Storage Mater.* **2018**, *10*, 206–215.
- [14] Y. Feng, H. Liu, F. Zhao, Y. Liu, J. Li, X. Liu, *Chem. Eng. J.* **2021**, *409*, 128177.
- [15] C. Wang, Y. Yi, H. Li, P. Wu, M. Li, W. Jiang, Z. Chen, H. Li, W. Zhu, S. Dai, *Nano Energy* **2020**, *67*, 104253.
- [16] Y. Zheng, Y. Yi, M. Fan, H. Liu, X. Li, R. Zhang, M. Li, Z.-A. Qiao, *Energy Storage Mater.* **2019**, *23*, 678–683.
- [17] T. Shi, C. Zhao, Y. Zhou, H. Yin, C. Song, L. Qin, Z. Wang, H. Shao, K. Yu, *J. Colloid Interface Sci.* **2021**, *599*, 416–426.
- [18] B. Yan, X. Li, W. Xiao, J. Hu, L. Zhang, X. Yang, *J. Mater. Chem. A* **2020**, *8*, 17848–17882.
- [19] W. Chen, H. Jin, S. Xie, H. Xie, J. Zhu, H. Ji, L.-J. Wan, *J. Energy Chem.* **2021**, *54*, 16–22.
- [20] Z. Fan, C. Zhang, W. Hua, H. Li, Y. Jiao, J. Xia, C.-N. Geng, R. Meng, Y. Liu, Q. Tang, Z. Lu, T. Shang, G. Ling, Q.-H. Yang, *J. Energy Chem.* **2021**, *62*, 590–598.
- [21] R. Saroha, J. H. Oh, Y. H. Seon, Y. C. Kang, J. S. Lee, D. W. Jeong, J. S. Cho, *J. Mater. Chem. A* **2021**, *9* (19), 11651–11664.
- [22] H. Zhang, S. Xin, J. Li, H. Cui, Y. Liu, Y. Yang, M. Wang, *Nano Energy* **2021**, *85*, 106011.
- [23] P. Cheng, P. Guo, K. Sun, Y. Zhao, D. Liu, D. He, *J. Membr. Sci.* **2021**, *619*, 118780.
- [24] J. Liu, Q. Zhang, Y.-K. Sun, *J. Power Sources* **2018**, *396*, 19–32.
- [25] H. Yuan, J.-Q. Huang, H.-J. Peng, M.-M. Titirici, R. Xiang, R. Chen, Q. Liu, Q. Zhang, *Adv. Energy Mater.* **2018**, *8*, 1802107.
- [26] L. Wang, Y. Ye, N. Chen, Y. Huang, L. Li, F. Wu, R. Chen, *Adv. Funct. Mater.* **2018**, *28*, 1800919.
- [27] Y. Li, C. Wang, W. Wang, A. Y. S. Eng, M. Wan, L. Fu, E. Mao, G. Li, J. Tang, Z. W. Seh, Y. Sun, *ACS Nano* **2020**, *14*, 1148–1157.
- [28] Y. Li, W. Wang, B. Zhang, L. Fu, M. Wan, G. Li, Z. Cai, S. Tu, X. Duan, Z. W. Seh, J. Jiang, Y. Sun, *Nano Lett.* **2021**, *21*, 6656–6663.
- [29] Y. Li, J. Wu, B. Zhang, W. Wang, G. Zhang, Z. W. Seh, N. Zhang, J. Sun, L. Huang, J. Jiang, J. Zhou, Y. Sun, *Energy Storage Mater.* **2020**, *30*, 250–259.
- [30] S. Deng, Q. Li, Y. Chen, C. Wang, H. Zhao, J. Xu, J. Wu, X. Yao, *Inorganic Chem. Frontiers* **2021**, *8*, 1771–1778.
- [31] Z. Sun, T. Wang, Y. Zhang, K. Kempa, X. Wang, *Electrochim. Acta* **2019**, *327*, 134843.
- [32] J. He, L. Luo, Y. Chen, A. Manthiram, *Adv. Mater.* **2017**, *29*, 1702707.
- [33] Y. Liu, X. Qin, S. Zhang, G. Liang, F. Kang, G. Chen, B. Li, *ACS Appl. Mater. Interfaces* **2018**, *10*, 26264–26273.
- [34] J. Balach, J. Linnemann, T. Jaumann, L. Giebeler, *J. Mater. Chem. A* **2018**, *6*, 23127–23168.
- [35] X. Liu, J.-Q. Huang, Q. Zhang, L. Mai, *Adv. Mater.* **2017**, *29*, 1601759.
- [36] D. Li, J. Yang, X. Xu, X. Wang, J. Chen, J. Xu, N. Zhao, *J. Membr. Sci.* **2020**, *611*, 118300.
- [37] J. Park, K. An, Y. Hwang, J. G. Park, H. J. Noh, J. Y. Kim, J. H. Park, N. M. Hwang, T. Hyeon, *Nat. Mater.* **2004**, *3*, 891–8955.
- [38] Z. Shi, M. Li, J. Sun, Z. Chen, *Adv. Energy Mater.* **2021**, *11*, 2100332.
- [39] Z. Shi, Z. Sun, J. Cai, X. Yang, C. Wei, M. Wang, Y. Ding, J. Sun, *Adv. Mater.* **2021**, *33*, 2103050.

Manuscript received: January 10, 2022
Revised manuscript received: January 30, 2022
Accepted manuscript online: February 10, 2022
Version of record online: February 24, 2022